Supporting Information

Ring Polymer Molecular Dynamics in Gas Surface Reactions: Inclusion of Quantum Effects Made Simple

Qinghua Liu[1], Liang Zhang[1], Yongle Li[2,*], Bin Jiang[1,*]

[1]*Hefei National Laboratory for Physical Science at the Microscale, Department of Chemical Physics, Key Laboratory of Surface and Interface Chemistry and Energy Catalysis of Anhui Higher Education Institutes, University of Science and Technology of China, Hefei, Anhui 230026, China*

[2] *Department of Physics, International Center of Quantum and Molecular Structures and Shanghai Key Laboratory of High Temperature Superconductors, Shanghai University, Shanghai 200444, China.*

*: corresponding authors: yongleli@shu.edu.cn, bjiangch@ustc.edu.cn

I. Computational Details

A. Potential energy surfaces

Two benchmark systems have been tested in this work, namely H_2+Cu(111) and D_2O+Ni(111). Within the Born-Oppenheimer static surface (BOSS) approximation, the corresponding potential energy surfaces (PESs) are represented by six and nine molecular degrees of freedom (DOFs), respectively. The Jacobi coordinates of the two systems are depicted in Fig. S1. For H_2+Cu(111), we use an analytical London-Eyring-Polanyi-Sato (LEPS) PES of Dai and Zhang[1] that was parameterized with limited density functional theory (DFT) data. The DFT calculations were based on the generalized gradient approximation (GGA)[2] (but with the densities calculated from local density approximation) and pseudopotentials with a four layer Cu(111) slab. The classical dissociation barrier height for bridge site is lowest (0.72 eV), followed by the hollow (0.90 eV) and top sites (1.14 eV). Including zero point energies (ZPEs) of the reactant and transition state, the lowest ZPE corrected barrier over the bridge site becomes 0.65 eV. A two-dimensional (2D) cut of the PES is displayed in Fig. S2a, as a function of Z and r with the molecule parallel to the surface at the bridge site dissociating to the two hollow sites.

For D_2O+Ni(111), there has been a first-principles nine-dimensional (9D) PES of Jiang and Guo[3] that was accurately fitted to over 25000 DFT data in terms of the permutation invariant polynomial neural network (PIP-NN) approach[4]. The DFT data was generated at the GGA level with the Perdew-Wang (PW91) functional[2] using a 4-

layer Ni(100) slab and 3×3 unit cell. The site-specific classical barrier height on this PES ranges from 0.67 to 0.87 eV[3]. The lowest transition state is nearby the top site and the ZPE corrected activation barrier is 0.58 eV[3]. A 2D PES contour plot is shown in Fig. S2b, as a function of Z and r_2 with molecular center of mass (COM) fixed at the transition state and other angular DOFs optimized. More details of the two PESs can be found in the original publications[1, 3].

B. Quasi classical trajectory

The quasi classical trajectory (QCT) method is a standard approach to involve the initial quantization of reactants in molecular dynamics simulations. Our QCT calculations were performed with the VENUS program[5] heavily modified by us for gas-surface scattering[4]. For H_2+Cu(111), the H_2 molecule is treated as rotating oscillator, whose internal energy is determined by Einstein–Brillouin–Keller (EBK) semiclassical method[6] with given vibrational and rotational quantum numbers v and j. Specifically, the EBK semi-classical method gives us the rovibrational energy of H_2 (E_{vj}) and the inner (r_-) and outer (r_+) turning points. A random distance r within [r_-, r_+] interval is selected, and its corresponding vibrational momentum is calculated by $p_r = \sqrt{2\mu\left[E_{vj} - E_r(r) - V(r)\right]}$, where $E_r(r) = j^2 / 2\mu r^2$ and $V(r)$ are the rotational and potential energy of H_2 at a bond length of r, μ is the reduced mass. Since the probability of a particular r is proportional to the inverse of p_r[7], namely $P(r) \propto 1/p_r$, an (r, p_r) pair is accepted only if $P(r)/ P^0(r) > R$, where R is a random number, and $P^0(r)$

is calculated by p_r for the most probable r (*i.e.* the turning point)[8]. The vibrational phase is determined by another random number R', whether $R'>0.5$ (positive) or $R'<0.5$ (negative). Indeed, the EBK semiclassical quantization for H_2 reproduces the quantum energy levels quite accurately (see Table S1). The initial (X, Y) coordinates of the H_2 COM was randomly chosen in a unit cell and Z is fixed at 8 Å above the surface. The initial polar and azimuthal angles (θ, φ) are also randomly sampled. The initial COM translational momentum is along surface normal. A trajectory is deemed as reactive if the H-H distance is larger than 2.5 Å and as scattered if the molecule is 8.1 Å above the surface with a velocity away from the surface.

For D_2O+Ni(111), the molecular COM and orientation are sampled in the same way as for H_2+Cu(111). Standard normal mode sampling is employed to prepare the ground state of D_2O or a collection of internal states based on the Boltzmann probabilities of them at given temperature (T_g = 300 K, here). A trajectory is deemed reactive if the longer O-D distance is larger than 2.2 Å and scattering if the molecule is 8.1 Å above the surface with a velocity away from the surface. In both systems, the propagation is performed with a time interval of 0.1 fs using the velocity Verlet algorithm until the trajectory reaches either the dissociation or the scattered channel. The initial sticking probability (S_0) can be calculated as $S_0=N_r/N_{tot}$, where N_r represents the number of reactive trajectory, and N_{tot} is the number of total effective trajectory.

C. Ring polymer molecular dynamics

As discussed in the main text, the ring polymer molecular dynamics (RPMD) theory is established on an isomorphism from the equilibrium quantum mechanical partition function to the classical partition function of a fictitious ring polymer[9]. The corresponding equilibrium RPMD Hamiltonian is extracted from the expression of partition function as[10],

$$H_P(\mathbf{p},\mathbf{q}) = \sum_{k=1}^{P}\sum_{j=1}^{N}\left[\frac{(\mathbf{p}_j^k)^2}{2m_j} + \frac{1}{2}m_j\omega_P^2(\mathbf{q}_j^k - \mathbf{q}_j^{k-1})^2\right] + \sum_{k=1}^{P}V(\mathbf{q}_1^k, \mathbf{q}_2^k, ..., \mathbf{q}_N^k) \qquad (1)$$

where N and P are the number of atoms in the system and beads in the ring polymer, $\mathbf{p}_j^k$ and $\mathbf{q}_j^k$ are the momentum and position vectors of the kth bead of the ring polymer representing the jth atom and $\mathbf{q}_j^0 = \mathbf{q}_j^P$, V is the PES depending on the positions of the same numbering of the beads for all atoms, m_j is the jth atomic mass that is used for each bead of this atom, and ω_P is the frequency harmonic potential taking the value of $\omega_P = P/\beta$ ($\beta = 1/kT$). The time evolution of the RPMD Hamiltonian is then fully determined by the classical dynamics so that the coordinate and momentum of each bead are propagated by,

$$\dot{\mathbf{p}}_j^k = \frac{\partial H_P(\mathbf{p},\mathbf{q})}{\partial \mathbf{q}_j^k}$$

$$\dot{\mathbf{q}}_j^k = \frac{\partial H_P(\mathbf{p},\mathbf{q})}{\partial \mathbf{p}_j^k} \qquad (2)$$

The corresponding RPMD time correlation function in equilibrium conditions well approximates the quantum counterpart and even becomes exact in several important limits, including short time, high temperature, and harmonic interaction potentials[11].

For describing the gas-surface collision process with a specific incidence energy, we have to use the non-equilibrium RPMD (NE-RPMD) Hamiltonian[12],

$$H'_P(\mathbf{p},\mathbf{q}) = \sum_{k=1}^{P}\sum_{j=1}^{N}\left[\frac{(\mathbf{p}_j^k - \Delta\mathbf{p})^2}{2m_j} + \frac{1}{2}m_j\omega_P^2(\mathbf{q}_j^k - \mathbf{q}_j^{k-1})^2\right] + \sum_{k=1}^{P}V(\mathbf{q}_1^k, \mathbf{q}_2^k, ..., \mathbf{q}_N^k) \quad (3)$$

where an initial momentum impulse Δp is added that corresponds to the initial translational energy given in molecular beam experiments. Miller and coworkers[12] have shown that several limits of equilibrium RPMD time correlation functions are preserved in non-equilibrium conditions and RPMD is able to achieve similar accuracy for calculating equilibrium and non-equilibrium correlation functions. For our purpose, it is also important that RPMD intrinsically incorporates zero point energy (ZPE) of the system, preserves the quantum Boltzmann distribution at a given temperature[11], and avoids unphysical ZPE leakage by construction[13]. One can estimate the internal energy of the ring polymer system from the centroid virial theorem[14],

$$< E >= \frac{3N}{2\beta} + < \frac{1}{2P}\sum_{k=1}^{P}\sum_{j=1}^{N}(\mathbf{q}_j^k - \bar{\mathbf{q}}_j)\frac{\partial V(\mathbf{q}_1^k, \mathbf{q}_2^k, ..., \mathbf{q}_N^k)}{\partial \mathbf{q}_j^k} > + < \frac{1}{P}\sum_{k=1}^{P}V(\mathbf{q}_1^k, \mathbf{q}_2^k, ..., \mathbf{q}_N^k) > \quad (4)$$

where $\bar{\mathbf{q}}_j = \sum_{k=1}^{P}\frac{\mathbf{q}_j^k}{P}$ representing the position of centroid.

Our NE-RPMD simulations of gas-surface reactions are implemented in two stages, namely thermalization (NVT ensemble) of the reactants and collision dynamics (NVE ensemble), following the recent work of Suleimanov and coworker[15]. We first run equilibrium path integral molecular dynamics (PIMD) of the gaseous reactant coupled with a thermostat at a given gas temperature (T_g = 300 K, here). Here, the bead positions

are assembled in the equilibrium geometry of the molecule far above the surface and their momenta are randomly sampled from the Maxwell-Boltzmann distribution at T_g = 300 K. The trajectory is propagated with velocity Verlet algorithm and a time step of 0.1 fs. These beads become naturally scattered once propagated and form ring polymers, because of the inter-bead harmonic potentials. The momentum of each bead is resampled every 10 fs due to the Andersen thermostat[16]. Note that the COM translational energy of the reactant is removed, which is equivalent to imposing a constraint on the reaction coordinate as in the calculation of rate constants[17]. The system accommodates to the given temperature typically within 1 ps, after which the trajectory snapshots are stored every 3 fs (30 steps). This equilibration procedure is an essential stage to ensure ergodicity in PIMD[18]. As a result, these snapshots include bead positions and momenta that can be used as initial conditions for the subsequent collision dynamics simulation. In addition, the molecular COM is randomly placed in the unit cell at Z = 8 Å above the surface. An additional momentum pointing to the surface along surface normal is added to each bead for a given normal incidence energy (or the translational energy) E_n, namely $\Delta\mathbf{p}_j^k = -m_j\sqrt{2E_i / M}$. These trajectories are then propagated without a thermostat and each atom is assumed to be located at the centroid of the corresponding ring polymer so as to decide whether the trajectory is reactive or not. The criteria for reactive and scattered trajectories are exactly the same as those given above for QCT calculations.

D. Quantum dynamics

Our quantum dynamics (QD) calculations have been done with the time-dependent wavepacket method, which has been detailed in Refs. [19] and [20]. Briefly, within the BOSS approximation, the quantum wave packet is represented by six and nine Jacobi coordinates in the H_2+Cu(111) and D_2O+Ni(111) systems, as illustrated in Fig. S1. The uniform quantum Hamiltonian of a molecule-surface system can be written as,

$$\hat{H} = \hat{K}_{trans} + \hat{K}_{vib} + \hat{K}_{rot} + \hat{V}(\mathbf{q}), \tag{5}$$

where $\hat{K}_{trans}$ is the three-dimensional kinetic energy operator (KEO) for the center-of-mass translation ($\hbar$=1 hereafter),

$$\begin{aligned} \hat{K}_{trans} &= -\frac{1}{2M}\left(\frac{\partial^2}{\partial Z^2} + \frac{\partial^2}{\partial X^2} + \frac{\partial^2}{\partial Y^2}\right) \\ &= -\frac{1}{2M}\left(\frac{\partial^2}{\partial Z^2} + \frac{1}{\sin^2\gamma}\frac{\partial^2}{\partial u^2} + \frac{1}{\sin^2\gamma}\frac{\partial^2}{\partial v^2} - \frac{2\cos\gamma}{\sin^2\gamma}\frac{\partial^2}{\partial u \partial v}\right). \end{aligned} \tag{6}$$

Here, Z and (X, Y) correspond to perpendicular and parallel translation of the molecule, γ is the skew angle between two lattice vectors (u, v) and M is the molecular mass. On the other hand, $\hat{K}_{vib}$ and $\hat{K}_{rot}$ represent the vibrational and rotational KEOs of the molecule, respectively. The vibrational KEO depends on both the intramolecular radial and angular coordinates, while the rotational KEO depends on angular variables that describe the rotation and orientation of the molecule, as illustrated in Fig. S1. $\hat{V}(\mathbf{q})$ is the molecule-surface interaction PES depending on all coordinates. Specifically, for the H_2+Cu(111) system, $\hat{K}_{vib} + \hat{K}_{rot}$ can be expressed as,

$$\hat{K}_{vib}+\hat{K}_{rot}=-\frac{1}{2\mu}\frac{\partial^2}{\partial r^2}+\frac{\hat{j}^2}{2\mu r^2}, \tag{7}$$

where μ is the reduced mass of H_2, $\hat{j}$ is the angular momentum of H_2, r is the H-H bond length. For the D_2O+Ni(111) system, , $\hat{K}_{vib}+\hat{K}_{rot}$ can be expressed as,

$$\hat{K}_{vib}+\hat{K}_{rot}=-\frac{1}{2\mu_1}\frac{\partial^2}{\partial r_1^2}-\frac{1}{2\mu_2}\frac{\partial^2}{\partial r_2^2}+\frac{\hat{j}^2}{2\mu_1 r_1^2}+\frac{\left(\hat{J}-\hat{j}\right)^2}{2\mu_2 r_2^2}, \tag{8}$$

where r_1 is the bond length of the non-dissociative OD bond, r_2 the distance between COM of OD and D, the corresponding reduced masses are $\mu_1=m_D m_O/(m_D+m_O)$, $\mu_2=m_{OD}m_D/(m_{OD}+m_D)$, $\hat{j}$ and $\hat{J}$ are the OD and D_2O angular momentum operators, respectively.

The wave function is expanded by the radial and rotational basis functions. Specifically, sine basis functions are used for the translational coordinate Z, which is divided into the interaction and asymptotic regions, in order to take advantage of an L grid saving scheme. Periodic Fourier functions are used for for u and v. The vibrational basis along r_i (r for H_2+Cu system and i =1 or 2 for D_2O+Ni system) consists of the reference vibrational eigenfunctions $\phi_{n_i}(r_i)$ for the one-dimensional reference Hamiltonian for the isolated molecule far from the surface, which satisfy the equation,

$$\left[-\frac{1}{2\mu_i}\frac{\partial^2}{\partial r_i^2}+V_{r_i}(Z_\infty,r_i,...)\right]\phi_{n_i}(r_i)=\varepsilon_n\phi_{n_i}(r_i). \tag{9}$$

For the H_2+Cu(111) system, a non-direct product FBR consisting of spherical harmonics $Y_j^{m_j}(\theta,\varphi)$ is employed to represent the angular wave function. While for the D_2O+Ni(111) system, The overall rotational basis is described by $Y_{jl}^{JM}(\theta_1,\theta_2,\varphi,\phi)$,

which is defined as,

$$Y_{jl}^{JM}(\theta_1,\theta_2,\varphi,\phi)=\sum_K D_{MK}^{J*}(\phi,\theta_2,\varphi)\sqrt{\frac{2l+1}{4\pi}}<jKl0\,|\,JK>y_{jK}(\theta_1,0), \qquad (10)$$

where $D_{MK}^{J}(\phi,\theta_2,\varphi)$ is the Wigner rotation matrix which can be expressed as $\sqrt{\frac{2J+1}{8\pi^2}}e^{-iM\phi}d_{MK}^{J}(\theta_2)e^{-iK\varphi}$, $y_{jK}(\theta_1,0)$ is the spherical harmonics. K and M are the projections of J on r_2 and the surface normal, respectively.

The initial normal-incident wave packet located in the reactant asymptote ($Z = Z_i$) as a product of a Gaussian wave packet in Z and internal state wavefunction of the reactant $|\psi_{\text{int}}\rangle$,

$$|\Psi_i(t=0)\rangle = Ne^{-(Z-Z_i)^2/2\delta^2}e^{-ik_iZ}|\psi_{\text{int}}\rangle, \qquad (11)$$

where the wave vector k_i is determined by the incidence energy E_i: $k_i=\sqrt{2ME_i}$, Z_i and δ are the initial central position and width of the Gaussian wave packet. The wave function was propagated using the split-operator method and absorbing potential was imposed at the edges of the grid to avoid spurious reflections,

$$D(\zeta)=\exp\left[-C_\zeta\left(\frac{\zeta-\zeta_a}{\zeta_{\max}-\zeta_a}\right)^2\right], \quad \zeta = Z \;\; or \;\; r_i. \qquad (12)$$

The initial state-selected reaction probability (P_0, or S_0 for molecular initial sticking probability) is obtained by evaluating the energy dependent reactive flux at the dividing surface ($r = r_f$, r is the dissociation bond),

$$P_0(E)=\frac{1}{\mu}\text{Im}\left\langle\psi_{iE}^{+}\left|\delta(r-r_f)\frac{\partial}{\partial r}\right|\psi_{iE}^{+}\right\rangle_{r=r_f}, \qquad (13)$$

where $\left|\psi_{iE}^{+}\right\rangle$ is the time-independent wave function which is related to time-dependent wave packet by a half Fourier transformation.

It should be noted that the nine-dimensional QD calculations for the D_2O+Ni(111) system are still extremely expensive. Instead, we take advantage of the site-averaging model proposed by Zhang and coworkers, which has been extensively tested for HCl+Au(111)[21], H_2 on Cu(111) and Ag(111)[22-23], and H_2O+Cu(111)[24] and H_2O+Ni(111)[25]. A simpler but relevant sudden approximation for averaging the site specific reactivity has already been applied by Jackson and coworkers in their reaction path Hamiltonian calculations even earlier[26]. In these activated systems, it has been validated that the exact full-dimensional dissociation probabilities can be well represented by the weighted sum of reduced-dimensional fixed-site ones with a sufficiently larger number of sites. The two sets of results are almost identical, implying negligible errors of this site-averaging approximation. The validity of the site-averaged model is on the basis of the fact that the dynamical steering is minor in these activated systems[23]. In our D_2O+Ni(111) PES, two hollow sites, *i.e.* the fcc and hcp sites, are indistinguishable due to the approximate C_{6v} symmetry enforced. This approximation, which is justified because of the negligibly small energy differences between the two sites[25], allows us to focus on an irreducible triangular region of the unit cell, shown in Fig. S1c. We compute the fixed-site seven-dimensional QD reaction probabilities up to 15 sites displayed in Fig. S1c to converge the nine-dimensional S_0 for D_2O on Ni(111).

To achieve numerical convergence, for H_2+Cu(111), the two dimensional unit cell

(u, v) is covered by a 14 × 14 evenly spaced Fourier grid. We use 127 sine basis functions ranging from 1.0 to 16.0 bohr for Z with 35 basis functions in the interaction region. 6 vibrational basis functions for r are used in the asymptotic region, while 30 in interaction region ranging from 0.5 to 6.0 bohr. The rotational basis is determined by $j_{\max} = 30$, $m_{j_{\max}} = 20$. The imaginary absorbing potentials are placed in the range of Z between 12.0 and 16.0 bohr and r between 4.0 and 6.0 bohr, respectively. The dissociation flux is calculated on the dividing surface of r = 3.5 bohr. The time step is 10 a.u. and we propagate the wave packets for 15000 a.u. of time to converge the dissociation probabilities. For D_2O+Ni(111), a total of 300 sine basis functions ranging from 2.0 to 17.0 bohr are used for Z with 130 basis functions in the interaction region, and 6 vibrational basis functions for both r_1 and r_2 were used in the asymptotic region, while 30 for r_2 in interaction region ranging from 1.0 to 5.5 bohr allowing for dissociation. The rotational basis set is defined by $J_{\max} = 37$, $l_{\max} = 35$, $K_{\max} = 27$ and $M_{\max} = 12$. The flux is analyzed at $r_{2f} = 3.6$ bohr and the damping function that absorbs the wave packet at the edges of the grid starts from Z = 15.0 bohr and r_2 = 3.7 bohr. The time step for the propagation is 10 a.u. and the wave packets is propagated up to 22000 a.u. in order to converge the reaction probability. We note that the final reaction probabilities obtained in the wave packet calculations are multiplied by a factor of 2 to account for the two equivalent O-D bonds.

The initial state selected wavepacket method only yields the reaction probability for a specific initial state. To get the thermally averaged reaction probability, one needs to consider the Boltzmann distribution of internal states at a given temperature T_g. The

thermally averaged reaction probability can be written as[27],

$$P(E_i;T_g)=\sum_{v,j}F_B\left(v,j;T_g\right)P_0\left(v,j;E_i\right). \tag{14}$$

Here, $P_0\left(v,j;E_i\right)$ is the initial state selected reaction probability and $F_B\left(v,j;T_g\right)$ is the Boltzmann weight of each rovibrational state, which is given by,

$$F_B\left(v,j;T_g\right)=w(j)(2j+1)\exp\left(-\beta E_{vj}\right)/N, \tag{15}$$

where the normalization factor N is the sum of all $F_B\left(v,j;T_n\right)$ terms, E_{vj} is the rovibrational energy relative to the ground state. In particular, $w(j)$ is a degeneracy factor due to the nuclear spin statistics of H_2 and D_2O, which is correlated with the corresponding rotational states. $w(j)$ is 1 for para-H_2 (even j states) and 3 for ortho-H_2 (odd j states). D_2O is an asymmetric top with its rotational state labeled as $J_{K_aK_c}$ and v_3 being the quantum number of antisymmetric stretch, for which the ortho and para states take the odd and even values of the sum (K_a+K_c+v_3) and their degeneracy factors are $w(j)$=2 and $w(j)$=1, respectively. The quantum internal energy (QIE) at a given temperature is also calculated in the same way by the thermal average over possible energy levels according to their Boltzmann weights,

$$\left\langle E_Q\right\rangle=\sum_{v,j}F_B\left(v,j;T_g\right)E_{vj}. \tag{16}$$

It should be noted that the conventional PIMD theory assumes all atoms as distinguishable and cannot take the nuclear spin statistics of ortho/para H_2 and D_2O into account. This assumption corresponds to an identical factor $w(j)$ to all states, or equivalently removing this factor from Eq. (15). We will discuss the effects of neglecting nuclear spin statistics in calculating QIEs and thermally averaged S_0 values below.

II. Additional results

We used the standard procedure to overcome the non-ergodicity of PIMD, which was first proposed by Pérez *et al.*[18]. As discussed in a recent review[11], because of the frequencies between beads of the ring-polymer depend on *P*, these springs between neighboring beads would become rigid with the increasing P, causing the non-ergodicity[28]. One way to overcome this difficulty is to run a set of short NVE trajectories initiated from uncorrelated snapshots sampled from a thermostatted (NVT) PIMD simulation. This procedure not only correctly samples the Boltzmann weight in the correlation function, but also ensures that each new NVE trajectory explores a different region of microcanonical phase space[11]. Although originally proposed for calculating correlation functions, this procedure has been successfully used in recent direct dynamics simulations[15, 29], giving rise to the proper initial conditions for NVE dynamics calculations. To check this ability, we plot in Fig. S3 the initial distributions of θ and φ of H_2 of NVE trajectories, extracted from snapshots after the 1 ps equilibrium PIMD, where the position of a hydrogen atom is given by its centroid. It is found that the angular distributions are generally isotropic within statistical errors, indicating that the H_2 molecule is randomly sampled with respect to its orientation. We also check the initial positions and momenta in the phase space for each degree of freedom of each H atom (too many, not shown), which fulfill a Gaussian distribution. This is consistent with what needs to be done in QCT calculations before collision.

Any path integral based method becomes increasingly accurate as *P* increases. Fig. 1 in the main text shows that the PIMD internal energy of the molecule at moderate and

high temperatures converges quickly with P. However, the discretization error of a path integral calculation is a function of β_P. We therefore also characterize the convergence of internal energy at a given temperature as a function of β_P (or equivalently PT_g), as shown in Fig. S4. One immediately realizes that the convergence of PIMD internal energy at low temperature requires much larger number of beads. We further show the convergence behavior of S_0 with respect to P in Fig. S5, which is found to be similar to that of internal energy, namely S_0 is also converged with P = 40 for H_2+Cu(111) and P = 30 for D_2O+Ni(111).

It is well-known that the antisymmetric requirement of the total wavefunction of Fermions results in a 3:1 ratio of ortho (odd j) and para (even j) states of H_2, and a 2:1 ratio of ortho (K_a+K_c+v_3=odd) and para (K_a+K_c+v_3=even) states of D_2O. It has been found that there is little need to distinguish the different nuclear spin species, in case of a simulation at high temperature, for example, for liquid H_2O at room temperature[30] or for rate constants of F+H_2 and H+H_2 reactions above 200 K[31]. In Fig. S6, the QIEs calculated with and without considering this nuclear spin statistics are compared. There are some very minor differences (< 5 meV) at low temperatures (T_g < 200 K) for H_2, and the two sets of results become increasingly indistinguishable with the increasing temperature. For D_2O, the difference is negligible in the entire temperature range up to 300 K. At higher temperatures, it becomes difficult to assign the ortho and para states of D_2O, but we expect no visible difference there. As a result, we indeed show the QIE results without incorporating nuclear spin statistics in Fig. 1.

To converge the H_2 QD dissociative sticking probability on Cu(111) at T_g = 300 K,

we compute the state-specific S_0 up to $H_2(v = 0, j = 4)$. The results as a function of incidence energy are shown in Fig. S7a. It is found that S_0 becomes increasingly higher at low incidence energies with the increasing rotational quantum number. As a result, the thermally averaged S_0 values are slightly higher than the ground state ones at very low energies, as shown in Fig. 2 in the main text. Again, we see invisible difference between results with and without including the nuclear spin degeneracy factor of ortho/para H_2 (3:1), as displayed in Fig. S7b.

Next, we discuss a possible reason for the less satisfactory performance of RPMD at E_i =0.6~1.0 eV. Indeed, similar phenomenon has been observed in recent NE-RPMD calculations for H scattering on graphene[29], where the RPMD calculated sticking probabilities at high incidence energies are also generally lower than classical ones (note that there is no internal state and ZPE for hydrogen atom). These authors offered no explanation for this difference in that work. To overcome the dissociation barrier, the molecule has to approach the surface closely. However, a too close distance to the surface will cause too strong repulsive force that prevents molecular dissociation. In Fig. S8a, we compare the distributions of closest distance between the molecular center and the surface (Z_{min}) during QCT and RPMD nonreactive trajectories, at E_i=0.8 eV. It is found that the RPMD distribution obtained by taking the centroid of the ring polymer as the position of atomic hydrogen (referred as RPMD-cen), agrees well with the QCT counterpart. It should be noted, however, that the RPMD theory generates multiple replicas of the system and each of them is evolved in terms of the molecule-surface interaction potential. In this sense, we can evaluate Z_{min} from each replica of H_2 as well.

One can see in the same Figure that the RPMD distribution obtained by the minimum value of Z_{min} among all replicas (referred as RPMD-min), shifts apparently to the shorter distance end. This indicates that some H_2 replicas in RPMD simulations could move much closer to the surface exceeding the average distance described by the centroid. These beads may feel a strong repulsive force and drive the whole molecule back to the vacuum, thus decreasing the dissociation probability. This mechanism would be more important near the hollow site, where the molecule would more easily access to the surface. This hypothesis is confirmed in Fig. S8b by comparing the RPMD-min distributions of Z_{min} during trajectories initiated from the circles centered at the hollow and bridge sites, respectively, with a radius of 0.32 Å (sudden approximation works well in this system). The average minimum value of Z_{min} is smaller for the hollow (1.07 Å) than for the bridge site (1.17 Å). This is consistent with the much smaller S_0 at the hollow (0.28) than that at the bridge site (0.48) evaluated from these trajectories. By contrast, the QCT calculate S_0 are comparable at the two sites (0.54 and 0.65) by the same analysis. As a result, we attribute the underestimated S_0 by RPMD to the fact that some replicas access closer to the surface and feel stronger repulsive force than others to hinder the molecular dissociation. This effect should be less important in the case of D_2O because the heavy oxygen atom (and its replicas) would not approach closely to the surface in any way. It should be noted that this is just a reasonable and qualitative interpretation and more factors may be involved in this process.

Finally, taking the first bending state as an example, we clarify in Fig. S9a that how we scale the corresponding S_0 curve of with a varying vibrational efficacy η defined in the main text. The horizontal shift in translational energy (ΔE_i) between the ground and excited state S_0 curves is determined as $\Delta E_i = E_{vj} \times \eta$, where E_{vj} is the rovibrational excitation energy. A Boltzmann average over all possibly populated states at T_g = 300 K gives rise to the QD S_0 curve at this temperature, which is shown in Fig. S9b as a function of η, compared to the ground state QD S_0 curve and the RPMD S_0 values at T_g = 300 K. It is found that the thermal contribution due to internal excitation is important and should be included for a fair comparison with RPMD results. In addition, the S_0 curve does not change much with an η value close to 1, especially at high translational energies. Again, in Fig. S9c, one notes that the S_0 curves with and without including the nuclear spin degeneracy factor of ortho/para D_2O (2:1) are indistinguishable. In any case, the agreement between RPMD and QD results at T_g = 300 K is excellent. Also shown in Fig. S9b is the estimated QD S_0 values at T_g = 300 K by adding up the relative difference of QCT (T_g = 300 K) and QCT (ground state), namely S_0(QD, 300 K) = S_0(QD, ground state)×S_0(QCT, 300 K)/S_0(QCT, ground state). Interestingly, the two different ways to correct the thermal effect yield more or less the same results. The agreement with the RPMD and QD S_0 at T_g = 300 K validates the accuracy of RPMD simulations with respect to the inclusion of quantum effects.

Table. S1 Comparison of rovibrational energy levels (in eV) of H_2 obtained by EBK and QD calculations.

	v=0, j=0	v=0, j=1	v=0, j=2	v=0, j=3	v=0, j=4
EBK	0.268	0.284	0.313	0.357	0.415
QD	0.269	0.283	0.313	0.357	0.415

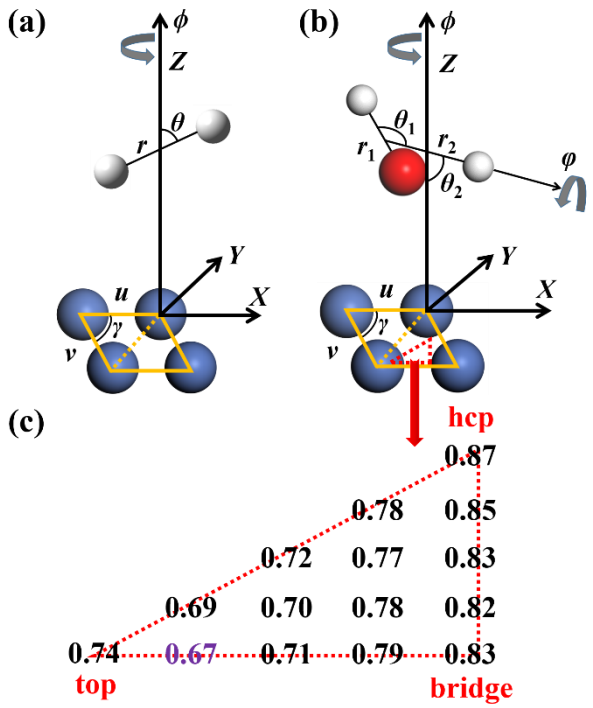

Fig. S1 Six (a) and nine (b) coordinates defined in our dynamical models for H_2+Cu(111) and D_2O+Ni(111) systems, respectively. (c) Schematic diagram indicating the 15 site positions and the classical barrier heights in the symmetry unique region of the unit cell used in the site-averaging model. The lowest barrier is marked in purple.

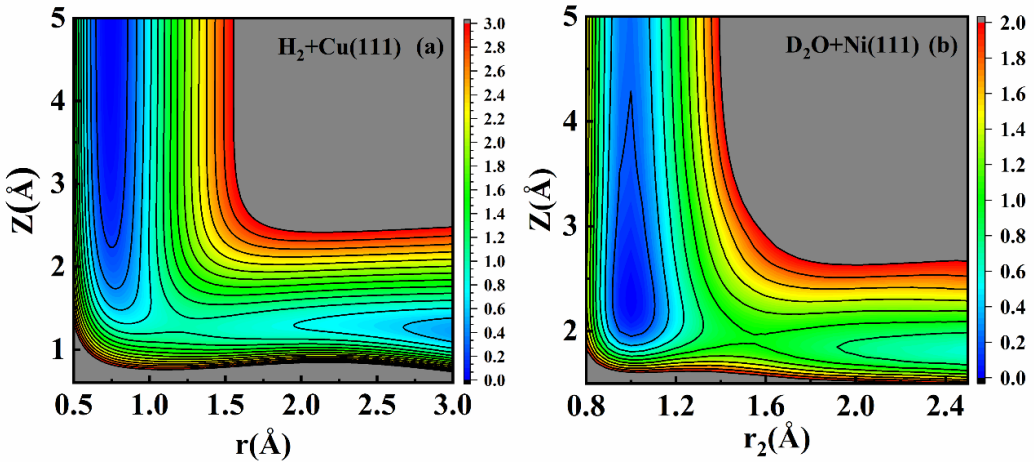

Fig. S2 Two dimensional contour plots of the potential for the H_2+Cu(111) (a) and D_2O+Ni(111) (b) systems as a function of the molecular height above the surface (Z) and the dissociating coordinate (r or r_2). The molecular center is fixed at the bridge site and with H_2 parallel to the surface dissociating to two hollow sites for H_2+Cu(111) and the molecular center is fixed at the transition state and with other angular DOFs optimized for D_2O+Ni(111).

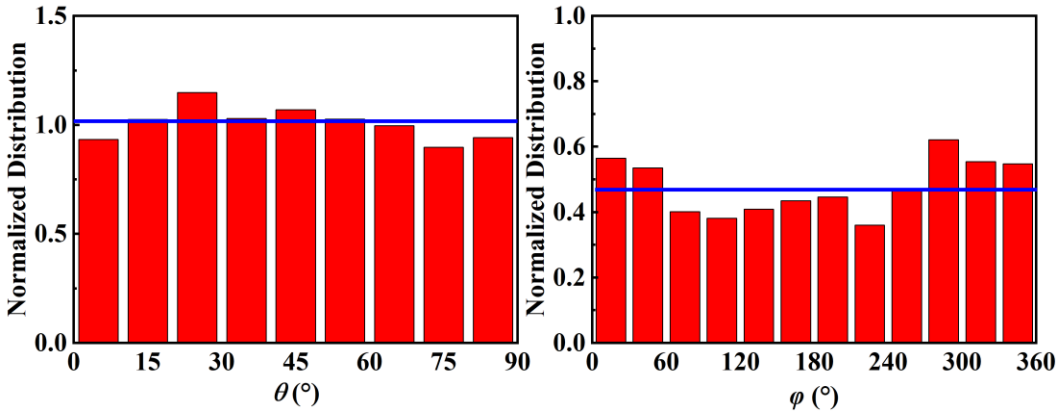

Fig. S3 Normalized distributions of polar angle P(θ) (a) and azimuth angle P(φ) (b) of initial H_2 configurations far from Cu(111) for the NE-RPMD simulations taken from equilibrated PIMD trajectories with the Andersen thermostat at temperature of 300 K. Note that P(θ) for polar angle is divided by the normalization factor sin(θ). The blue line corresponds to the theoretical uniform distribution as a guide of eyes.

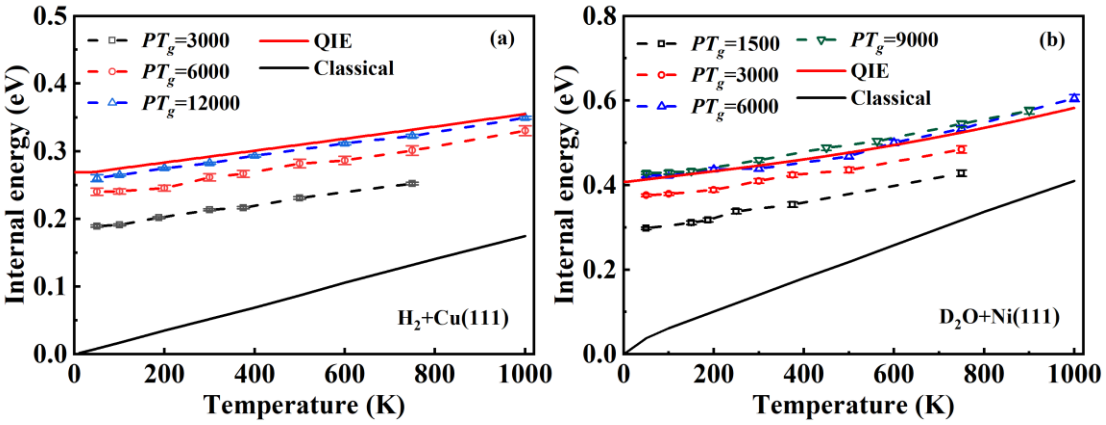

Fig. S4 PIMD internal energies of H_2 (a) and D_2O (b) estimated from NVT simulations of H_2+Cu(111) and D_2O+Ni(111) systems via virial centroid theorem, as a function of temperature at fixed β_P (equivalently PT_g) values, compared to classical (black line) and quantum internal energy (red line).

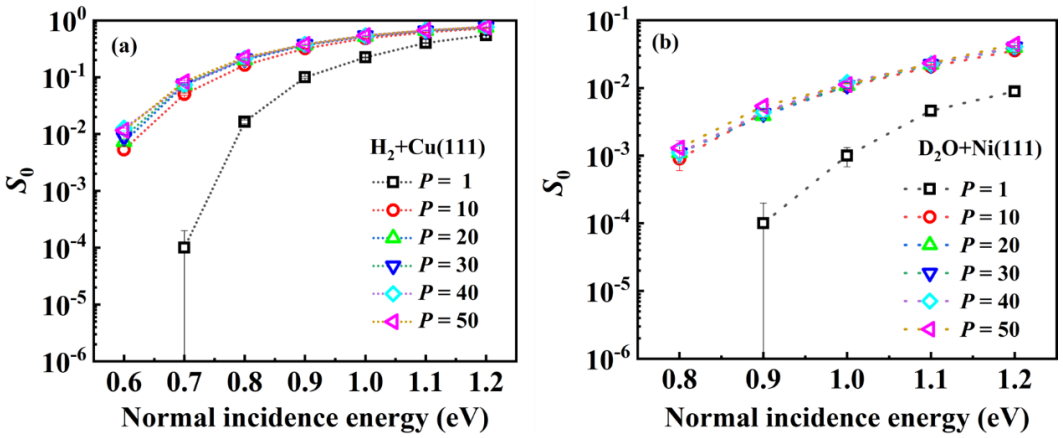

Fig. S5 Dependence of S_0 on the number of beads for H_2 on Cu(111) (a) and D_2O on Ni(111) (b), at T_g= 300 K.

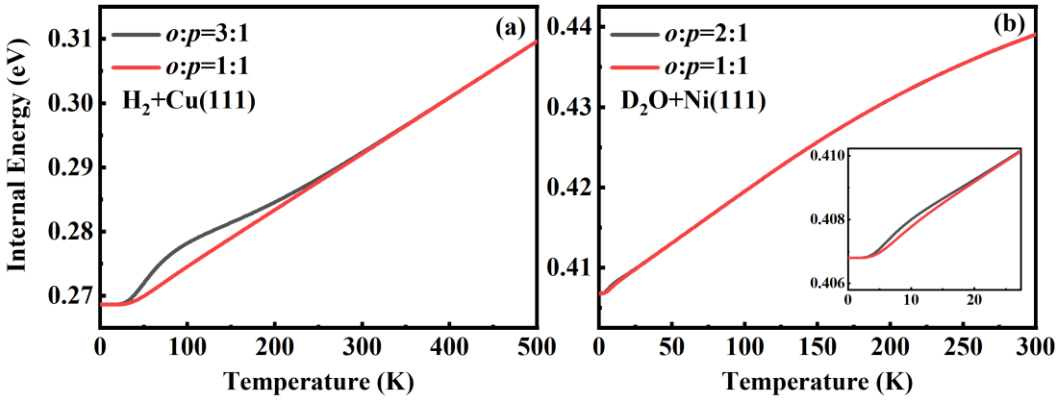

Fig. S6 Quantum internal energies of H_2 (a) and D_2O (b) calculated with (black) and without (red) consideration of nuclear spin statistics (ortho:para=3:1 for H_2 and 2:1 for D_2O). The inset of panel (b) illustrates the subtle difference of two sets of calculations at very low temperature.

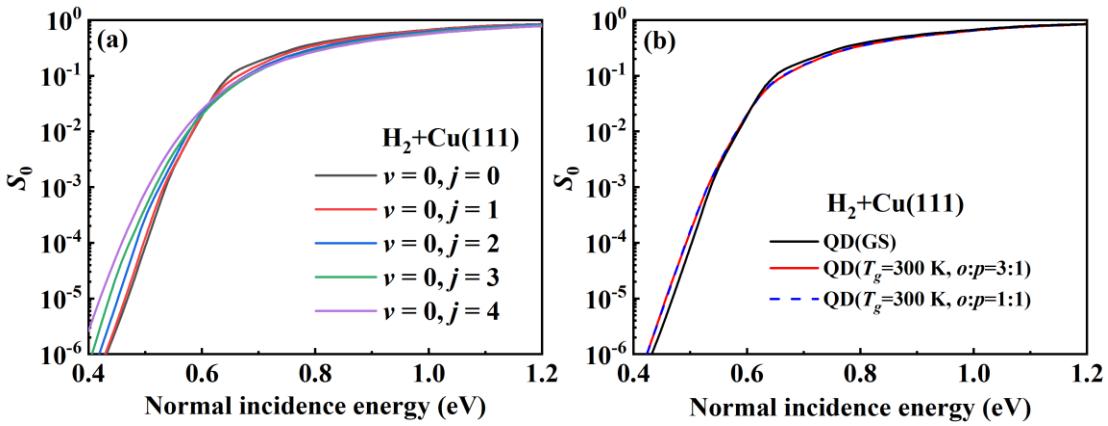

Fig. S7 (a) State selected dissociation probabilities for H_2(v = 0, j = 0-4) on Cu(111). (b) thermally averaged dissociation probabilities at T_g= 300 K calculated with (red solid) and without (blue dash) consideration of nuclear spin statistics (ortho:para=3:1 for H_2), compared with the ground state reactivity (black solid) of H_2 on Cu(111).

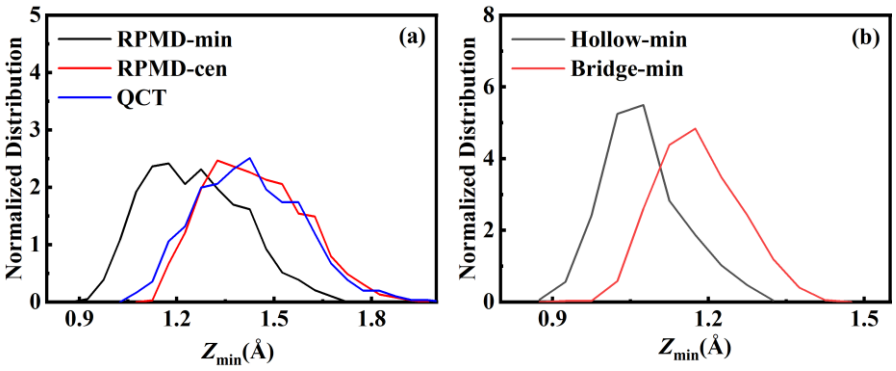

Fig. S8 (a) Distributions of the closest vertical distance between H_2 and the Cu(111) surface (Z_{min}) during scattered trajectories obtained from QCT (blue), RPMD with the center of centroid (RPMD-cen, red), and RPMD with the minimum value of Z_{min} among all replicas (RPMD-min, black). (b) Comparison of RPMD-min distributions obtained with trajectories initiated in a region centered at the bridge site (red) and hollow site (black), respectively, with a radius of 0.32 Å.

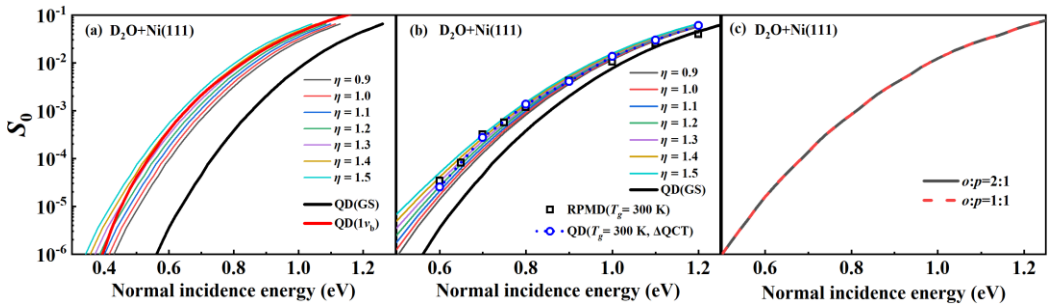

Fig. S9 (a) Approximate S_0 curves (thin lines) of the first bending excited state of D_2O ($1\nu_b$) shifted from the baseline of ground state (thick black line) by a varying vibrational efficacy (η), compared to the exact calculated S_0 curve of D_2O ($1\nu_b$) (thick red line). (b) Boltzmann average of QD S_0 curves over all possibly populated states at T_g=300 K with different universal η (thin lines). The QD S_0 curve for the ground state (thick black line), RPMD results (black squares), and QD results estimated from QCT at T_g=300 K (blue circle), are shown for comparison. (c) Boltzmann average of QD S_0 curves over all possibly populated states at T_g=300 K, obtained with (black line) and without (red dash line) considering nuclear spin statistics (ortho:para= 2:1 for D_2O).

References:

1. Dai, J.; Zhang, J. Z. H. Quantum adsorption dynamics of a diatomic molecule on surface: Four-dimensional fixed-site model for H_2 on Cu(111). *J. Chem. Phys.* **1995,** *102* (15), 6280-6289.
2. Perdew, J. P.; Wang, Y. Accurate and simple analytic representation of the electron-gas correlation energy. *Phys. Rev. B* **1992,** *45* (23), 13244–13249.
3. Jiang, B.; Guo, H. Dynamics of water dissociative chemisorption on Ni(111): Effects of impact sites and incident angles. *Phys. Rev. Lett.* **2015,** *114*, 166101.
4. Jiang, B.; Guo, H. Permutation invariant polynomial neural network approach to fitting potential energy surfaces. III. Molecule-surface interactions. *J. Chem. Phys.* **2014,** *141*, 034109.
5. Hu, X.; Hase, W. L.; Pirraglia, T. Vectorization of the general Monte Carlo classical trajectory program VENUS. *J. Comput. Chem.* **1991,** *12*, 1014-1024
6. Gutzwiller, M. C. *Chaos in Classical and Quantum Mechanics*. Springer: New York, 1990.
7. Porter, R. N.; Raff, L. M.; Miller, W. H. Quasiclassical selection of initial coordinates and momenta for a rotating Morse oscillator. *J. Chem. Phys.* **1975,** *63*, 2214.
8. Peslherbe, G. H.; Wang, H.; Hase, W. L. Monte Carlo sampling for classical trajectory simulations, a chapter in Monte Carlo methods in chemical physics. *Adv. Chem. Phys.* **1999,** *105*, 171-201.
9. Chandler, D.; Wolynes, P. G. Exploiting the isomorphism between quantum theory and classical statistical mechanics of polyatomic fluids. *J. Chem. Phys.* **1981,** *74*, 4078-4095.
10. Craig, I. R.; Manolopoulos, D. E. Quantum statistics and classical mechanics: Real time correlation frunction from ring polymer molecular dynamics. *J. Chem. Phys.* **2004,** *121*, 3368-3373.
11. Habershon, S.; Manolopoulos, D. E.; Markland, T. E.; Miller III, T. F. Ring-polymer molecular dynamics: Quantum effects in chemical dynamics from classical trajectories in a extended phase space. *Annu. Rev. Phys. Chem.* **2013,** *64*, 387-413.
12. Welsch, R.; Song, K.; Shi, Q.; Althorpe, S. C.; Miller, T. F. Non-equilibrium dynamics from RPMD and CMD. *J. Chem. Phys.* **2016,** *145* (20), 204118.
13. Habershon, S.; Manolopoulos, D. E. Zero point energy leakage in condensed phase dynamics: an assessment of quantum simulation methods for liquid water. *J. Chem. Phys.* **2009,** *131* (24), 244518.
14. Herman, M. F.; Bruskin, E. J.; Berne, B. J. On path integral Monte Carlo simulations. *J. Chem. Phys.* **1982,** *76* (10), 5150-5155.
15. Suleimanov, Y. V.; Aguado, A.; Gómez-Carrasco, S.; Roncero, O. A ring polymer molecular dynamics approach to study the transition between statistical and direct mechanisms in the $H_2 + H_3^+ \rightarrow H_3^+ + H_2$ reaction. *J. Phys. Chem. Lett.* **2018,** *9*, 2133-2137.
16. Andersen, H. C. Molecular dynamics simulations at constant pressure and/or temperature. *J. Chem. Phys.* **1980,** *72*, 2384-2393.
17. Suleimanov, Y. V.; Aoiz, F. J.; Guo, H. Chemical reaction rate coefficients from ring polymer molecular dynamics: Theory and practical applications. *J. Phys. Chem. A* **2016,** *120* (43), 8488-8502.
18. Pérez, A.; Tuckerman, M. E.; Müser, M. H. A comparative study of the centroid and ring-polymer molecular dynamics methods for approximating quantum time correlation functions from path integrals. *J. Chem. Phys.* **2009,** *130* (18), 184105.
19. Jiang, B.; Guo, H. Six-dimensional quantum dynamics for dissociative chemisorption of H_2 and D_2 on Ag(111) on a permutation invariant potential energy surface. *Phys. Chem. Chem. Phys.* **2014,** *16*, 24704-24715.
20. Jiang, B.; Song, H.; Yang, M.; Guo, H. Quantum dynamics of water dissociative chemisorption on rigid Ni(111): An approximate nine-dimensional treatment. *The Journal of Chemical Physics* **2016,** *144*

(16), 164706.
21. Liu, T.; Fu, B.; Zhang, D. H. Six-dimensional quantum dynamics study for the dissociative adsorption of HCl on Au(111) surface. *J. Chem. Phys.* **2013,** *139*, 184705.
22. Liu, T.; Fu, B.; Zhang, D. H. Validity of the site-averaging approximation for modeling the dissociative chemisorption of H_2 on Cu(111) surface: A quantum dynamics study on two potential energy surfaces. *J. Chem. Phys.* **2014,** *141*, 194302.
23. Hu, X.; Jiang, B.; Xie, D.; Guo, H. Site-specific dissociation dynamics of H_2/D_2 on Ag(111) and Co(0001) and the validity of the site-averaging model. *J. Chem. Phys.* **2015,** *143*, 114706.
24. Zhang, Z.; Liu, T.; Fu, B.; Yang, X.; Zhang, D. H. First-principles quantum dynamical theory for the dissociative chemisorption of H_2O on rigid Cu(111). *Nat. Comm.* **2016,** *7*, 11953.
25. Jiang, B.; Guo, H. Quantum and classical dynamics of water dissociation on Ni(111): A test of the site-averaging model in dissociative chemisorption of polyatomic molecules. *J. Chem. Phys.* **2015,** *143* (16), 164705.
26. Jackson, B.; Nave, S. The dissociative chemisorption of methane on Ni(100): Reaction path description of mode-selective chemistry. *J. Chem. Phys.* **2011,** *135*, 114701.
27. Diaz, C.; Olsen, R. A.; Busnengo, H. F.; Kroes, G.-J. Dynamics on six-dimensional potential energy surfaces for H_2/Cu(111): Corrugation reducing procedure versus modified Shepard interpolation method and PW91 versus RPBE. *J. Phys. Chem. C* **2010,** *114* (25), 11192-11201.
28. Hall, R. W.; Berne, B. J. Nonergodicity in path integral molecular dynamics. *J. Chem. Phys.* **1984,** *81* (8), 3641-3643.
29. Jiang, H.; Kammler, M.; Ding, F.; Dorenkamp, Y.; Manby, F. R.; Wodtke, A. M.; Miller, T. F.; Kandratsenka, A.; Bünermann, O. Imaging covalent bond formation by H atom scattering from graphene. *Science* **2019,** *364* (6438), 379.
30. Vega, C.; Abascal, J. L. F. Simulating water with rigid non-polarizable models: a general perspective. *Phys. Chem. Chem. Phys.* **2011,** *13* (44), 19663-19688.
31. Collepardo-Guevara, R.; Suleimanov, Y. V.; Manolopoulos, D. E. Bimolecular reaction rates from ring polymer molecular dynamics. *J. Chem. Phys.* **2009,** *130*, 174713.